Soft Matter

PAPER

View Article Online
View Journal | View Issue

Cite this: *Soft Matter*, 2020, **16**, 1227

Oscillations of a cantilevered micro beam driven by a viscoelastic flow instability

Anita A. Dey,[ab] Yahya Modarres-Sadeghi,[a] Anke Lindner[b] and Jonathan P. Rothstein *[a]

Received 4th September 2019,
Accepted 20th December 2019

DOI: 10.1039/c9sm01794a

rsc.li/soft-matter-journal

The interaction of flexible structures with viscoelastic flows can result in very rich dynamics. In this paper, we present the results of the interactions between the flow of a viscoelastic polymer solution and a cantilevered beam in a confined microfluidic geometry. Cantilevered beams with varying length and flexibility were studied. With increasing flow rate and Weissenberg number, the flow transitioned from a fore-aft symmetric flow to a stable detached vortex upstream of the beam, to a time-dependent unstable vortex shedding. The shedding of the unstable vortex upstream of the beam imposed a time-dependent drag force on the cantilevered beam resulting in flow-induced beam oscillations. The oscillations of the flexible beam were classified into two distinct regimes: a regime with a clear single vortex shedding from upstream of the beam resulting in a sinusoidal beam oscillation pattern with the frequency of oscillation increasing monotonically with Weissenberg number, and a regime at high Weissenberg numbers characterized by 3D viscoelastic instabilities where the frequency of oscillations plateaued. The critical onset of the flow transitions, the mechanism of vortex shedding and the dynamics of the cantilevered beam response are presented in detail here as a function of beam flexibility and flow viscoelasticity.

1 Introduction

Fluid–structure interactions (FSI) have been heavily studied by researchers because of their ubiquity in a variety of mechanical, industrial and biological processes. At high Reynolds numbers, the interaction of flexible structures with flow instabilities leads to very rich dynamics documented in many books and review papers.[1–7] In low Reynolds number flows, although flows are stable, complexity arises from non-linear interactions between deformable structures and viscous flow. Viscous fluid motion can modify the shape, orientation and position of a structure which in turn leads to coupling between the flow field and the structural response.[8] FSI studies of these flows are relevant to the biological and physiological world seen in the flow past flagella,[9] swimming of micro-organisms,[10] the deformation of red blood cells during transport in blood vessels[11] or the deformation of soft fluid-conveying vessels.[12,13] An important class of low Reynolds number flows includes viscoelastic fluid flows. In these flows, purely elastic instabilities can occur even in the absence of inertia[14–17] and can in turn interact with flexible structures. Although these elastic flow instabilities have been reported in a host of viscoelastic fluids and flow geometries, such viscoelastic FSI studies (VFSI) remain scarce and have only recently been conducted for the flow of wormlike micelle solutions past flexible structures placed in a crossflow.[18–20] However, the interplay between the various types of viscoelastic fluids, flexible structures and flow geometries is expected to lead to a large variety of dynamics, relevant for a number of fields such as low Reynolds number flows and structural mechanics.

Polymer solutions are often classified as viscoelastic fluids due to the complex behavior of these fluids imparted by the physical nature of a mobile polymer macromolecule. As a flexible polymer coil stretches within a flow field, it is deformed out of its equilibrium random walk configuration. An elastic restoring force results, driving the polymer back toward its entropically favorable equilibrium state.[21] High molecular weight polymers can thus impart an entropic elasticity to a fluid which allows the polymer solution or melt to carry stress along the flow streamlines and can lead to the build up of normal stresses in simple shear flows. The importance of elasticity in the flow is described by the non-dimensional Weissenberg number, $\mathrm{Wi} = \lambda\dot{\gamma}$, where λ is fluid relaxation time and $\dot{\gamma} = U/L$ is the shear rate, where U is the flow velocity and L is the characteristic lengthscale. The importance of inertia is described by the Reynolds number, $\mathrm{Re} = UL/\nu$, where ν is the kinematic viscosity of the fluid. High Weissenberg number flows have become easily achievable in the absence of inertia, $\mathrm{Re} \ll 1$, in microfluidics.[22] The micrometer sized flow

[a] *Department of Mechanical and Industrial Engineering, University of Massachusetts, Amherst, Massachusetts 01003, USA. E-mail: rothstein@ecs.umass.edu*
[b] *Laboratoire de Physique et Mécanique des Milieux Hétérogénes, UMR 7636, CNRS, ESPCI Paris, PSL Research University, Université Paris Diderot, Sorbonne Université, Paris 75005, France*

geometries result in large shear rates[23,24] and Weissenberg numbers while simultaneously minimizing the Reynolds number. The combination of large elastic stresses resulting from those high Weissenberg numbers and streamline curvature,[15,25] while keeping the Reynolds number small, leads to purely elastic flow instabilities, making these flows quite different from Newtonian fluid flows. The low Reynolds number-high Weissenberg number space that can be probed due to microfluidics has led to many studies of viscoelastic instabilities in polymer solutions. Various microfluidic geometries such as contraction–expansion flows,[26] cross-slot flows,[27,28] T-channel flows,[29] flow past cylinders[30] and serpentine channel flows[31] have been studied. Although all of these flows demonstrate the onset of elastic instabilities at large Weissenberg numbers, in all of the examples, the structure geometry is rigid and not actively interacting with the instabilities.

Alternatively, allowing these instabilities to affect the position, deformation and motion of an object falls in the domain of fluid–structure interaction problems and introduces a host of interesting questions regarding the dynamics and elasticity of the structures and boundaries of the flow. In this paper, using viscoelastic flow past a flexible beam attached as a cantilever to one side of a microchannel, we provide evidence that elastic flow instabilities occurring at high Weissenberg numbers in a confined flow of a polymer solution can, given the right structural flexibility, generate motion in the structure and subsequently couple with the structural motion.

The geometry of flexible beams used in this study has applications in the field of microfluidics in the development of micro- and nano-devices such as flow rate sensors and actuators.[32–35] Development of fluid-actuated cantilevered microscale beams to act as fluid energy harvestors is also a promising technology.[36] The results of this work could provide an insight into the use of viscoelastic flow instability as a mechanism of inducing vibrations in micro-structures. Thin flexible fibers are also commonly seen in biology, where they appear as cilia and flagella used for locomotion and feeding of various micro-organisms. Micro-organisms interact with biological flows which are often viscoelastic and always at low Reynolds numbers.[10,37] Mimicking of micro-organisms using bio-inspired cilia and flagella has applications in the development of artificial micro-swimmers, micro-pumps, valves and mixers.[38–40] Our study of thin cantilevered micro-scale beams placed in a viscoelastic polymer solution could help in understanding the dynamics and interactions of micro-organisms in a host of different micro-environments.

This paper describes the investigation of the flow of a viscoelastic polymer solution past a cantilevered beam attached to a side wall of a micro scale flow channel. The beam is confined by the top and bottom walls of the channel, occupying nearly the full channel depth and partially blocks the channel height due to its significant length. With increasing flow velocity, elastic instabilities arise in the flow due to the presence of the cantilevered beam which in turn begin to couple with the cantilevered beam. This interaction has been studied by varying the flexibility of the cantilevered beam placed in the flow path. The critical onset of beam oscillations, the underlying mechanism of the oscillations, the characteristics of the flow instabilities and the flow-induced beam deformation over a range of Weissenberg numbers are discussed. Across the tests of the cantilevered beams, two distinct regimes of the oscillatory response of the flexible beam are identified in this paper.

2 Experimental setup

The experimental geometry consisted of a long rectangular channel with a rectangular beam extending from one of the sidewalls (Fig. 1(left)). The channel was made of polydimethylsiloxane (polydimethylsiloxane, Sylgard 184, Corning) (PDMS) and fabricated using traditional soft-lithography techniques with a depth of d_c = 48 μm and heights of H = 150 μm and 360 μm. To fabricate the flexible beam, we used a stop flow microscope-based projection photolithography process[41,42] allowing for a precise control of beam shape and modulus. This method relies on the crosslinking of a photosensitive polymer solution inside a microfluidic channel under UV illumination through a mask. Crosslinking is hindered in the presence of oxygen as it quenches the photopolymerization reaction. PDMS being permeable to oxygen, using this method a beam cannot be directly attached to any of the walls of the microchannel. Instead, following Wexler *et al.*,[43] rectangular PDMS posts were fabricated close to the microchannel side wall which served as anchors for a rigid bounding sidewall, fabricated using the same projection photo-lithography process.[41,42] As a short segment in the sidewall and the beam are now made from the same material, the beam can be directly attached to the sidewall as shown in Fig. 1.

The microchannel was first filled with a photosensitive solution composed of 10 vol% of Darocur 1173 photo-initiator (PI, 2-hydroxy-2-methylpropiophenone, Sigma) and 90 vol% of polyethylene glycol-diacrylate (PEGDA, M_w = 700, Sigma). Under a zero flow condition, a photomask with the bounding wall geometry was placed in the field-stop position of a microscope

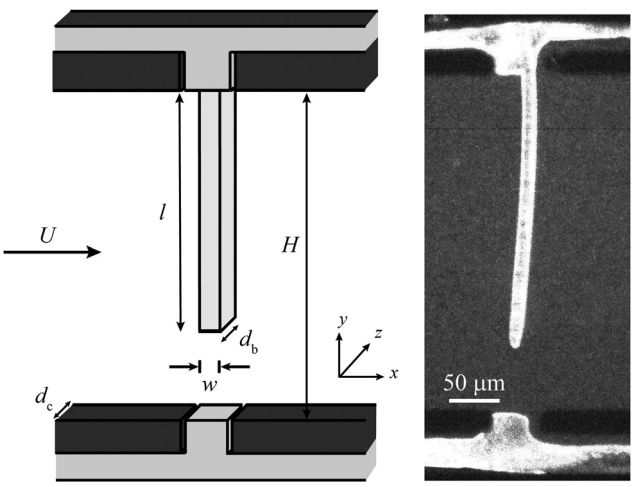

Fig. 1 A schematic diagram of the cantilevered beam in the microchannel is shown on the left. The dark gray areas are the sidewalls of the microchannel which are composed of PDMS. The light gray areas are the photo-polymerized bounding wall and the flexible cantilevered beam. An image of the beam in the microchannel is shown on the right.

(Zeiss) equipped with a UV light source (Lamp HBO 130W) and a 10× Fluar objective, and the shutter was opened for 800 ms. With an open shutter, the photosensitive solution in the microchannel exposed to UV light through the photo-mask underwent polymerization. Subsequently, a second photosensitive solution composed of 10 vol% Darocur 1173 photo-initiator (PI, 2-hydroxy-2-methylpropiophenone, Sigma), 45 vol% polyethylene glycol-diacrylate (PEGDA, M_w = 700, Sigma) and 45 vol% of a solvent mixture of water and polyethylene glycol (PEG, M_w = 1000, (Sigma) at a ratio of 1 : 2 in volume) was introduced into the microchannel for the fabrication of the flexible beam. A photo-mask of the beam geometry was placed at the base of the sidewall and allowed to photo-polymerize as described above. An image of the resulting cantilevered beam with a clamped boundary condition is shown in Fig. 1(right).

The photosensitive solution was then flushed to introduce the viscoelastic fluid into the microchannel. As the polymerized beam was exposed to the incoming aqueous viscoelastic solution, a swelling of the beam by 15% was observed for the flexible beams. The swelling of the beam in the microchannel was found to occur only at the initial inflow of the solution and no consequent changes in the polymerized beam were observed with time once the channel was filled with the aqueous polymer solution. The elastic moduli of the swollen flexible beam and bounding wall were determined outside the microfluidic device by measuring the deflection of a photo-polymerized beam under gravity after immersion in the aqueous polymer solution. The elastic modulii of the rigid bounding wall and flexible beam were found to be 12 MPa and 3 MPa, respectively. The non-polymerized layer above and below the swollen beam was measured to be 4 ± 1.5 μm.

Table 1 The beam length, l, channel height, H, channel blockage ratio at zero flow conditions, $\alpha = l/H$, beam stiffness, κ, and the range of the elasto-viscous numbers tested, $\tilde{\mu}$, of the fabricated beam geometries

	l [μm]	H [μm]	α	κ [N m^{-1}]	$\tilde{\mu}$
Beam 1	105 ± 2	150 ± 2	0.7	2×10^{-1}	2×10^{-4} to 1×10^{-2}
Beam 2	290 ± 2	360 ± 2	0.8	1×10^{-2}	1.2×10^{-3} to 1×10^{-1}

The relative intensity of viscous and elastic forces acting on the beam can be compared using a dimensionless elasto-viscous number, $\tilde{\mu} = \eta U l^3/EI$, where η is the fluid viscosity, U is a typical flow velocity, E is the material Young's modulus, I is the area moment of inertia.[8,44,45] The details of the fabricated beam geometries such as beam length, l, channel height, H, channel blockage ratio at zero flow conditions, $\alpha = l/H$, beam stiffness, $\kappa = EI/l^3$, and the range of the elasto-viscous numbers tested, $\tilde{\mu}$, are provided in Table 1. The channel depth, width and depth of the cantilevered beam, and elastic modulus were d_c = 48 ± 2 μm, w = 17 ± 2 μm, d_b = 40 ± 2 μm and E = 3 ± 0.2 MPa respectively. The theoretical natural frequency of the cantilevered beam in air was calculated to be $f_N \approx 1$ MHz which is much larger than any expected oscillation frequency in this experiment.[46] As a result, lock-in behavior often observed in Newtonian fluid–structure interactions is not anticipated.

The viscoelastic fluid was composed of Flopaam 3630 (SNF Floerger) mixed with deionized water at a concentration of 0.02 wt%. Flopaam is a partially hydrolyzed polyacrylamide with an extremely high molecular weight (20 MDa) and a degree of hydrolysis between 25–30%. At a concentration of 0.02 wt%, the mixture showed a zero shear rate viscosity of η_0 = 0.25 Pa s as shown in Fig. 2(a). Beyond a shear rate of $\dot{\gamma}$ = 1 s^{-1}, the steady shear rate viscosity was found to shear thin with a power law exponent of n = 0.3. The relaxation time of the fluid was measured in extensional flow using the capillary breakup extensional rheometer (CaBER) and was found to be λ = 0.05 s. CaBER can also be used to measure the extensional viscosity of the fluid.[47,48] The test fluid was found to be strain hardening with a steady-state extensional viscosity of η_E = 72 Pa s as seen in Fig. 2(b). The resulting Trouton ratio was found to be Tr = η_E/η_S = 288, which is significantly larger than the theoretical limit for a Newtonian fluid which is Tr = 3. This viscoelastic fluid is thus shear thinning, extensionally strain hardening and elastic.

A precision pump (Nemesys, Cetoni) was used to drive the flow in the microchannel at flow rates ranging from 0 to 150 nl s^{-1}. The flow experiments were recorded at a frame rate of 500 frames per second (Hamamatsu Orca-flash 4.0 camera). Particle image

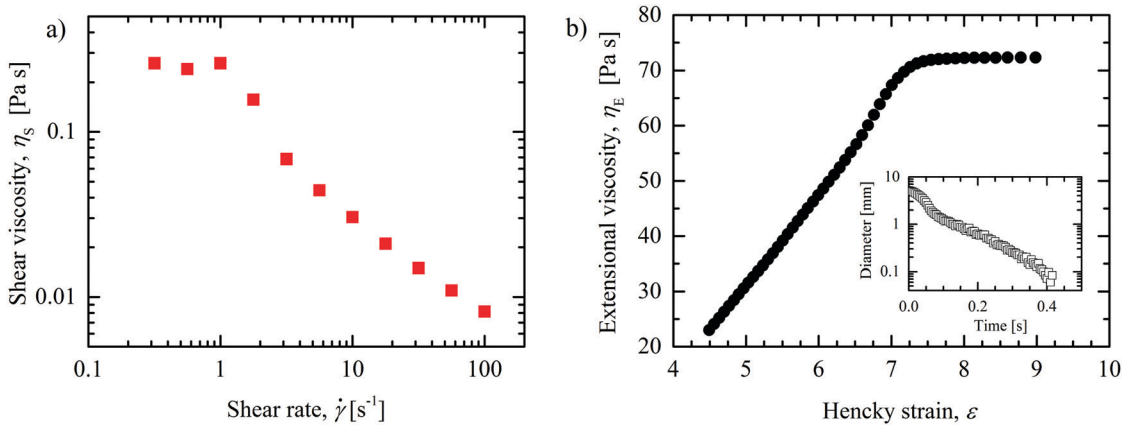

Fig. 2 (a) Shear viscosity as a function of the shear rate and (b) extensional viscosity *versus* Hencky strain of the viscoelastic polymer solution. The inset is a representative plot of the diameter decay *versus* time recorded in a CaBER experiment. The temperature of each experiment was T = 25 °C.

velocimetry was used to generate a complete and quantitative measurement of the velocity flow field around the cantilevered beam. The polymer solution was seeded with fluorescent microparticles of size 1 μm (Sigma Aldrich) at 0.005% by weight. The responses of the fabricated beams and the test fluid were analysed using a particle tracking software (Tracker), ImageJ (NIH) and the particle image velocimetry (PIV) technique (Lavision) respectively.

3 Results

In order to illustrate the response of the beam to the oncoming flow, a dimensionless Weissenberg number, $\mathrm{Wi} = \lambda U_{\mathrm{gap}}/d_{\mathrm{c}}$, is used where λ is the fluid relaxation time, d_{c} is the channel depth and U_{gap} is the average flow velocity in the gap between the tip of the beam and the opposite channel sidewall, neglecting leakage through the thin layer above and below the beam. This flow velocity in the gap is obtained as $U_{\mathrm{gap}} = Q/(d_{\mathrm{c}}(H - \bar{y}))$, where Q is the flow rate, d_{c} is the channel depth and $\bar{y}$ is the time-averaged projected length of the deformed beam perpendicular to the oncoming flow. This definition of the gap velocity ensures that the effects of increasing beam deformation with the flow rate and thus a flow-rate-dependent blockage ratio, $\alpha_{\mathrm{flow}} = \bar{y}/H$, are incorporated in the Weissenberg number.

The images in Fig. 3 represent the streakline and PIV images captured at Weissenberg numbers of Wi = 1.5 and Wi = 3 for stable flow past Beam 1 (see details in Table 1). At these flow rates, the cantilevered beam was observed to undergo a small static deformation in the flow direction, as observed by Wexler *et al.*[43] for a cantilevered beam in the flow of a Newtonian fluid. In Fig. 3(a) and (b), a small re-circulation zone can be observed just upstream of the cantilevered beam. The stability of the re-circulation zone can be confirmed by the streakline image taken over the course of a long exposure time of 0.5 s. This flow separation was found to be initiated at Weissenberg numbers of $\mathrm{Wi} \geq 1$. At these Weissenberg numbers, separated vortices upstream of flow obstacles have been observed in a number of viscoelastic microfluidic flows including flow into corners, into contractions and past posts.[26,49–52] All of these flows have the combination of streamline curvature and elasticity known to be necessary for elastic vortex formation.[15,25] This re-circulation zone was observed to increase in size with increasing flow velocity. As seen in Fig. 3, the vortex appears to originate at the corner between the beam and the upper wall. With increasing flow velocity, the vortex grows in size and intensity. Although the majority of the flow is deflected downward and around the tip of the cantilevered beam, a small fraction ($\approx$2%) of the flow can also be seen in the movies to pass through the small 4 μm gap between the beam and the upper and lower walls of the microchannel. At even higher flow velocities, the vortex upstream of the beam was found to become unstable and time dependent, which in turn triggered oscillations of the beam.

This flow transition was observed to occur at a Weissenberg number of $\mathrm{Wi}_{\mathrm{crit}} = 5$. The shedding of the unstable vortex was observed to produce periodic beam oscillations. A sequence of PIV images captured at time intervals of $\Delta t = 20$ ms at Wi = 16 for a shedding vortex are presented in Fig. 4. These PIV images illustrate the vortex evolution and the subsequent beam oscillations. In Fig. 4(a), the corner vortex at its maximum size can be seen at a location of about 100 μm upstream of the flexible beam. As time progressed from Fig. 4(b) to (c), the strength of the vortex, its vorticity, is observed to increase as the vortex center began to approach the flexible beam and move away from the wall. As time progresses further in Fig. 4(d), the center of the vortex is observed to move towards the tip of the flexible beam. At this position, the high flow velocity of the fluid passing around the tip of the cantilevered beam provides sufficient shear stress to dislodge the vortex, strip it from the beam and convect it downstream as seen in Fig. 4(e). In Fig. 4(f), the x-position of the cantilevered beam's tip is shown as a function of time. It is clear from Fig. 4(f) that the growth and decay of the vortex is directly coupled to oscillations observed at the tip of the cantilevered beam. The maximum deflection of the beam tip correlates with the instance shown in Fig. 4(c), when the center

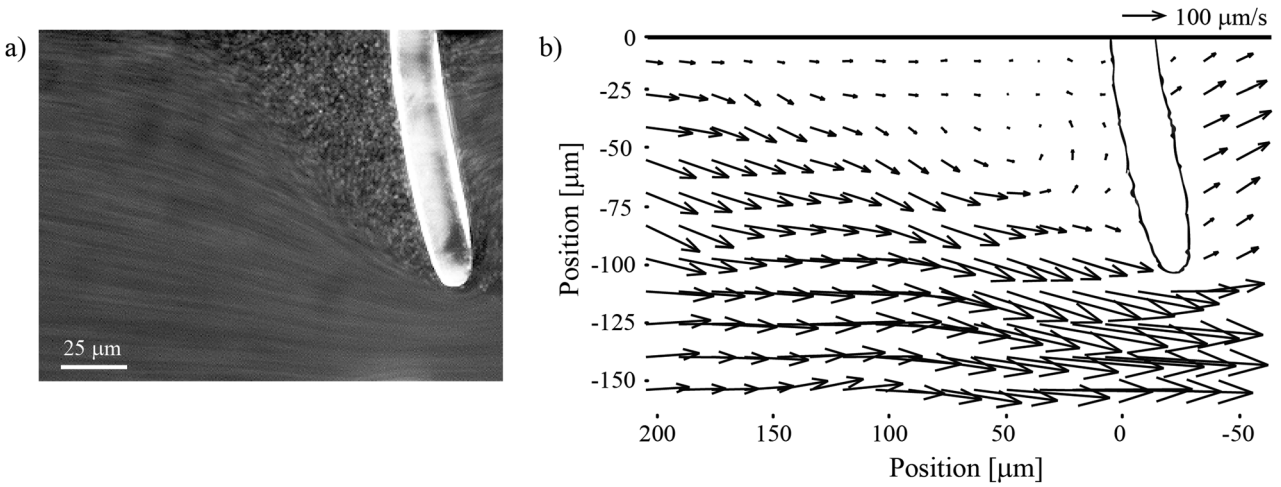

Fig. 3 The (a) darkfield streakline and (b) PIV images of viscoelastic flow past Beam 1 for Weissenberg numbers of (a) Wi = 1.5 and (b) Wi = 3. The flow is from left to right.

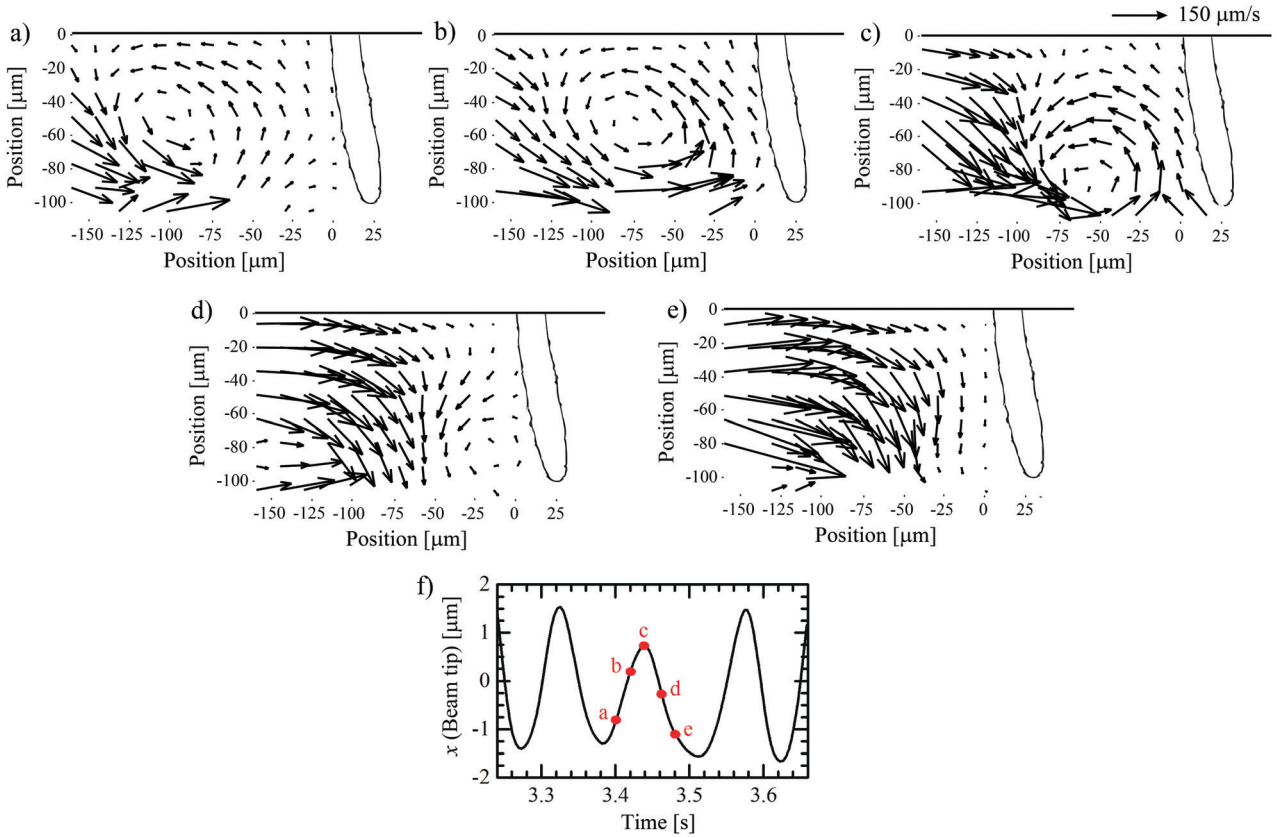

Fig. 4 (a–e) PIV image sequence for flow past Beam 1 at Wi = 16. The time interval between each two consecutive images is 20 ms. The flow is from left to right. (f) The time history of the beam tip displacement with the solid dots (●) corresponding to the PIV image sequence from (a) to (e).

of the vortex is at the same height as the tip of the beam, where the large torque arm helps maximize the deflection of the tip of the beam. The motion of the beam's tip in Fig. 4(f) appears to follow a sinusoidal motion with time. This motion is similar to the oscillations observed during vortex-induced vibration at high Reynolds numbers, but very different from the viscoelastic fluid–structure interactions previously observed for the flow of wormlike micelles past cylinders[19] or sheets.[18] In those systems, vortices upstream of the cylinder or sheet were not observed and instead, the oscillations were induced by a breakdown of the elastic fluid in the extensional flow region in the wake of the cylinder or sheet. The resulting oscillations followed a saw-tooth profile because the failure of the wormlike micelles that induced the observed flow instability was quite rapid.[19]

In Fig. 5(a), the oscillation frequency of the tip of Beam 1 and the frequency of velocity fluctuations a distance of $2w$ = 34 μm upstream of the tip of the beam are plotted against increasing Weissenberg number in the gap, Wi. The velocity fluctuations were obtained from PIV images. At the Weissenberg number of Wi = 5, the stable vortex upstream of the beam transitioned to an unstable time-dependent vortex resulting in a periodic shedding with a frequency of 2 Hz. The velocity fluctuations upstream of the beam resulting from the vortex shedding did not yet provide sufficient forcing to cause a time-dependent beam displacement that could be resolved at the magnification used in these experiments. A slight increase in the Weissenberg number led to the enhancement of the unstable vortex upstream of the beam and its subsequent shedding resulted in the onset of Beam 1 oscillations at the Weissenberg number of Wi = 10. Over most of the range where oscillations were observed, the frequency of the fluctuating velocity upstream of Beam 1 and the frequency of Beam 1 oscillations closely matched each other and increased monotonically with Weissenberg number (Fig. 5(a)). However, the beam oscillation frequency reached a plateau at Wi = 50 at about 33 Hz while the frequency of fluctuating velocity vectors continued to increase with Weissenberg number. As the natural frequency of the beam is many orders of magnitude larger than the frequency of observed beam oscillations, $f_N \approx 1$ MHz, the observed plateau is not associated with the lock-in observed for Newtonian FSI. At Wi > 50, the coherent vortices observed in Fig. 4 are no longer present upstream of the beam. The oscillations beyond this Weissenberg number are induced not by the shedding of a vortex with a single dominant frequency, but by 3D velocity fluctuations originating upstream and observed in the flow around the tip of the beam with a dominant frequency accompanied by higher harmonics exciting the motion of the beam. These 3D flow fluctuations around Beam 1 appear to be similar to the flow fluctuations observed for elastic turbulence at low Reynolds numbers.[53–55] A complex power spectra characteristic of elastic turbulence has been recently reported for the flow of wormlike micelle solutions past a microfluidic cylinder.[20] Unfortunately, the limitations of

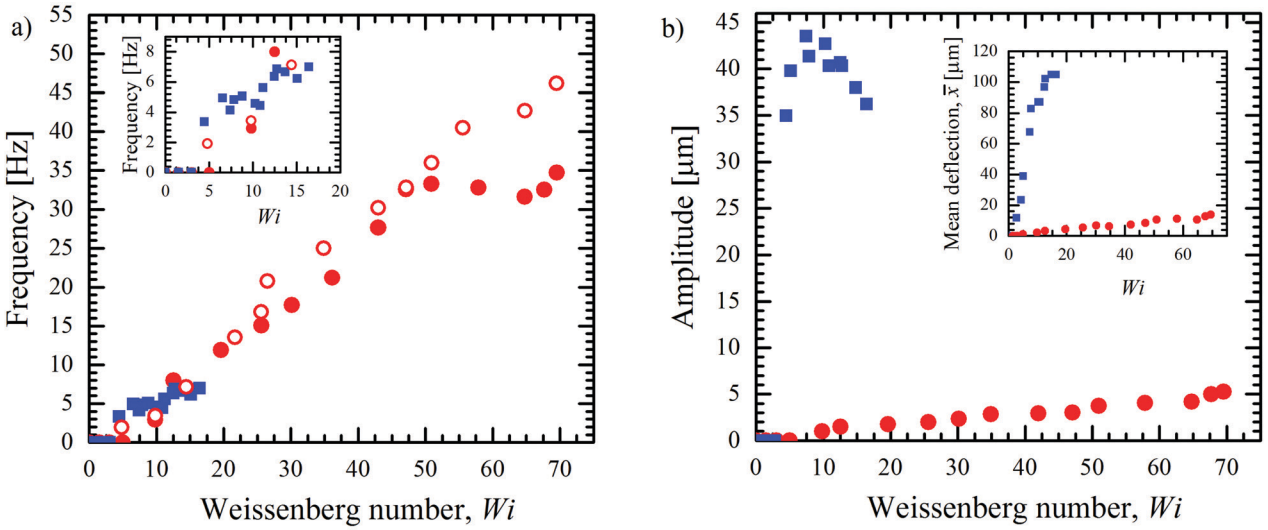

Fig. 5 (a and inset) Frequency of Beam 1 (●) and Beam 2 (■) along with the frequency of fluctuating velocity vectors obtained from PIV images at a point $2w$ = 34 μm upstream of the tip of Beam 1 (○) *versus* Weissenberg number. (b) Amplitude of Beam 1 (●) and Beam 2 (■) tip oscillations *versus* Weissenberg number. The inset is a plot of the mean deflection ($\bar{x}$) observed during oscillations *versus* Weissenberg number.

the current experimental setup do not allow a similar verification of the occurrence of elastic turbulence to be performed here. In Fig. 5(b), the amplitude of the Beam 1 tip oscillations and the mean beam deflection ($\bar{x}$) are plotted against increasing Weissenberg number. Even though the frequency plateaus beyond Wi > 50, the amplitude of oscillations and the mean beam deflection were observed to increase monotonically with the Weissenberg number reaching a maximum amplitude A = 5 μm at the highest Weissenberg number tested, Wi = 70.

A second set of experiments was conducted where the flexible Beam 1 was replaced with a more flexible beam, Beam 2 (see details in Table 1) which had the same beam width and elastic modulus but a longer beam length while maintaining a similar channel blockage ratio. By increasing the beam length while keeping other parameters constant, Beam 2 is an order of magnitude more flexible than Beam 1 resulting in a significantly larger mean deflection under the same flow conditions as seen in the inset of Fig. 5(b). The frequency and amplitude of Beam 2 oscillations are plotted over a range of Weissenberg numbers in Fig. 5(a) and (b). Similar to the case of Beam 1, a re-circulation zone was observed to grow upstream of Beam 2 at low flow velocities while the beam maintained a constant static deflection. The transition from a stable vortex to an unstable time-dependent vortex shedding was observed to occur at a similar Weissenberg number to that for Beam 1, *i.e.* Wi = 4. Accompanying the vortex shedding was the onset of periodic oscillations of Beam 2. The increased flexibility of Beam 2 was observed to have a significant impact on the beam oscillations as the agreement in the critical Weissenberg numbers between the two beams was only possible if the experimentally measured blockage ratio was used to calculate the effective shear rate between the tip of the beam and the bottom wall of the channel. Similar to Beam 1, the frequency of Beam 2 oscillations was observed to increase monotonically with the Weissenberg number.

The mechanism of the instability driving the beam oscillations differed slightly in the case of Beam 2 due to its increased flexibility. Unlike the vortex shedding pattern observed for Beam 1, the vortex upstream of Beam 2 was not observed to shed around the tip of the beam en masse. Two streakline images of the flow field upstream of Beam 2 in Fig. 6 show the complex flow conditions occurring during the beam oscillations (Wi = 8). The two instances occur at a time interval of Δt = 2.5 ms. In Fig. 6(a), a large re-circulating vortex can be observed upstream of Beam 2. Due to the increased beam length, the large vortex is observed to split in two with separate vortices appearing at the tip and the base. The two separate vortices were significantly smaller than the single vortex with some of the fluid shedding around the tip and some flowing through the 4 μm gap above and below the beam. This alternate vortex shedding pattern was observed during the Beam 2 oscillations up to a Weissenberg number of Wi = 12. The appearance of a smaller vortex near the tip of Beam 2 is similar to the lip vortices observed in studies of axisymmetric contraction–expansion flows with rounded corners where rounding of the corner led to a reduction in the contraction ratio and extensional stresses developed in the contraction.[56,57]

The amplitude of oscillations of Beam 2 was found to be significantly larger than that of Beam 1, reaching a maximum amplitude of A = 44 μm at Wi = 8, but then decaying with increasing Weissenberg number. Due to the increased flexibility of Beam 2, the beam underwent a significant beam deflection with increasing flow velocity. The progression of Beam 2 oscillations with increasing Weissenberg number is presented in Fig. 7. The vortex previously observed near the tip of Beam 2 is completely swept off of the beam at these high flow velocities as the beam curvature is unable to support the growth of vortices upstream of the beam and instead, the shear flow along the length of the beam sweeps them off along the beam. The large beam deflection and beam curvature observed in Fig. 6 and 7 are analogous to the

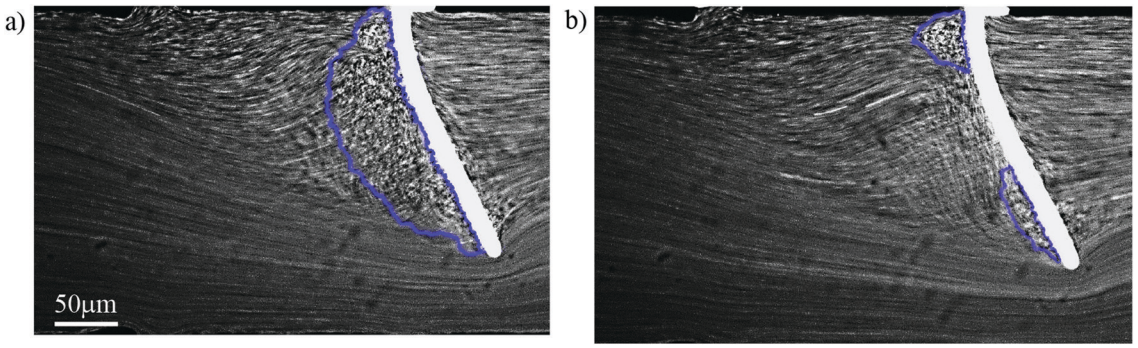

Fig. 6 Dark field streakline images of flow fluctuations occurring in the upstream region of Beam 2 at Wi = 8 for a time interval of 2.5 ms. The flow is from left to right.

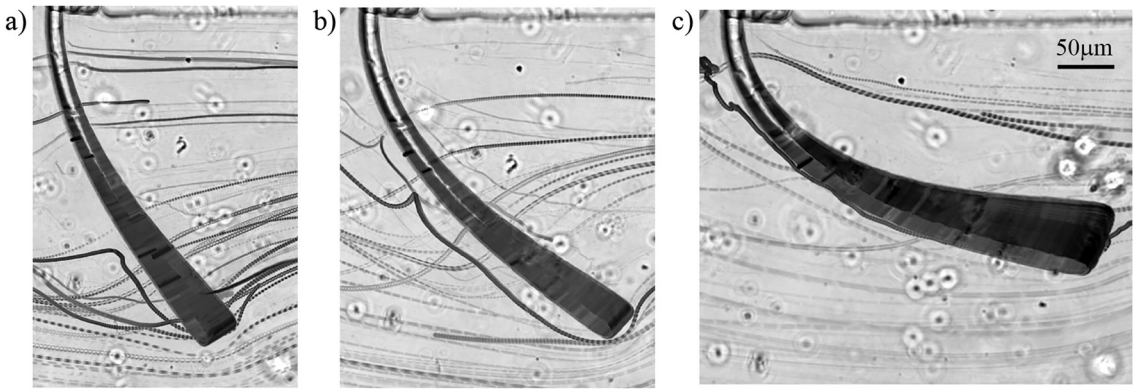

Fig. 7 Bright field streakline image of viscoelastic flow past Beam 2 at varying Weissenberg numbers. (a) Wi = 5, (b) Wi = 8 and (c) Wi = 12. The flow is from left to right.

curvature of re-entrant corners into planar and axisymmetric contractions.[56–58] As with the rounded re-entrant corners, the beam deflection and curvature resulted in a smoothing out of the streamlines leading to a reduction in the local Weissenberg number for the flow along the deflected beam span.[56–58] This further leads to a reduction of the local extension rate and extensional strain experienced by the polymer solution.[59] The elastic stress of the fluid passing between the tip of the beam and the opposite channel wall will thus be reduced leading to a decrease in the size of the expected re-circulation zone upstream of the beam and additionally, the amplitude of the beam oscillations. In Fig. 7, the displacement of the beam's tip can be seen as a broadening of the beam cross-section in the long time exposure images. The tip of the deflected beam can be observed to become almost parallel to the flow. A concentration of elastic stresses around the tip of slender objects in viscoelastic flows has been observed in numerical simulations.[60] A similar stress accumulation around the beam tip may be present here and contribute to the beam oscillations. Several traces of the flow path of the light-reflective particles are visible in these images. Traces of particles can be observed approaching the upstream face of the flexible beam, and then moving alongside the length of the flexible beam to slip off the beam edge into the flow. There are also traces of particles visible that move over and under the beam through the small gap between the beam and top and bottom walls.

The differences in the oscillation amplitudes between the two beams arise from the increased flexibility and the resulting larger mean beam deflection of Beam 2. For a cantilevered beam under a uniformly distributed load, the maximum tip deflection is given by $\delta_{max} = qL^4/8EI$, where $q = F/L$ is a uniformly distributed load,[61] that stems from the viscous and pressure forces of the viscous flow.[44,62] The exact pre-factors depend on the specific flow geometry and have been evaluated for the cantilevered beam and the confined geometry.[43] For constant channel and fiber geometry, blockage ratio, elastic and viscous properties, this equation can be simplified to, $\delta_{max} \sim L^3$. The Beam 2 deflection will be theoretically scaled by $(l_2/l_1)^3 = 21$, where l_1 and l_2 are the beam lengths of Beam 1 and Beam 2 respectively. This simplification agrees closely with the mean beam deflection during Beam 2 oscillations observed in the experiments.

4 Conclusions

We report the results of our viscoelastic–fluid structure interaction study of a microscale cantilevered beam subjected to the flow of a polymer solution. The interaction of the elastic flow instabilities with the cantilevered beam was studied on beams with varying flexibility. The flexibility of the beams was modified

by increasing the beam length while maintaining the same channel blockage ratio. The critical Weissenberg number at the onset of the spatio-temporal variation of the re-circulation zone upstream of the beam was found to $Wi_{crit} = 4$. The resulting oscillations of the flexible cantilevered beams, triggered by the shedding of the unstable vortex, were observed to display two distinct regimes. The first regime in which the amplitude and frequency of beam oscillations increased with the Weissenberg number was characterized by the shedding of either a single vortex for a less flexible beam or the splitting and then shedding of the upstream vortex as the beam flexibility increased. A second regime was observed where the frequency of oscillations plateaued with increasing Weissenberg number. This second regime of beam oscillations was characterized by 3D viscoelastic instabilities and the absence of a clear upstream vortex. The evolution of the upstream recirculating zone was found to be coupled with the flow-induced deformation and flexibility of the beam. We show that the mechanism of vortex shedding across a flexible structure is heavily influenced by the structural properties such as beam length and flexibility. The critical onset, frequency and amplitude of structural oscillations are a result of the strong coupling between the elastic flow instability and the intrinsic structural flexibility. We report the evidence of viscoelastic fluid–structure interactions in a confined flow of a polymer solution which vastly differentiates the resulting beam oscillation pattern from those previously reported for un-confined flows of worm-like micelle solutions. These conclusions illustrate the complex nature of viscoelastic–fluid structure interactions and the future possibilities of tuning of the microfluidic flow and/or geometric parameters.

Conflicts of interest

There are no conflicts to declare.

Acknowledgements

This work was funded by the National Science Foundation under grant CBET-1705251. AL and AAD acknowledge funding from the ERC Consolidator Grant PaDyFlow under Grant Agreement no. 682367 and support from the Institut Pierre-Gilles de Gennes (Équipement d'Excellence, ''Investissements d'avenir'', program ANR-10-EQPX-34). The authors would like to thank Jean Cappello and Lucie Ducloué for their help with the fabrication process of the flexible beams.

Notes and references

1 P. W. Bearman, *Annu. Rev. Fluid Mech.*, 1984, **16**, 195–222.
2 R. D. Blevins, *Flow-induced vibration*, Krieger Pub. Co., Malabar, Fla., 1990.
3 M. P. Païdoussis, *Fluid–Structure Interactions: Slender Structures and Axial Flow*, Academic Press Inc., San Diego, CA, 1998, vol. 1.
4 M. Païdoussis, *Fluid–Structure Interactions: Slender Structures and Axial Flow*, Academic Press, London, 2004, vol. 2.
5 M. P. Païdoussis, S. J. Price and E. de Langre, *Fluid–Structure Interactions – Cross-Flow-Induced Instabilities*, Cambridge University Press, New York, 2011, vol. 1.
6 T. Sarpkaya, *J. Fluids Struct.*, 2004, **19**, 389–447.
7 C. H. K. Williamson and R. Govardhan, *Annu. Rev. Fluid Mech.*, 2004, **36**, 413–455.
8 O. Du Roure, A. Lindner, E. N. Nazockdast and M. J. Shelley, *Annu. Rev. Fluid Mech.*, 2019, **51**, 539–572.
9 C. Brennen and H. Winet, *Annu. Rev. Fluid Mech.*, 1977, **9**, 339–398.
10 E. Lauga and T. R. Powers, *Rep. Prog. Phys.*, 2009, **72**, 096601.
11 M. Abkarian and A. Viallat, *On the importance of the deformability of red blood cells in blood flow*, Royal Society of Chemistry, 2016, pp. 347–362.
12 M. Heil and A. L. Hazel, *Annu. Rev. Fluid Mech.*, 2011, **43**, 141–162.
13 C. Bertram, *Flow past highly compliant boundaries and in collapsible tubes*, Springer, 2003, pp. 51–65.
14 E. S. G. Shaqfeh, *Annu. Rev. Fluid Mech.*, 1996, **28**, 129–185.
15 G. H. McKinley, P. Pakdel and A. Öztekin, *J. Non-Newtonian Fluid Mech.*, 1996, **67**, 19–47.
16 R. Larson, *Rheol. Acta*, 1992, **31**, 213–263.
17 A. Groisman and V. Steinberg, *Nature*, 2000, **405**, 53–55.
18 A. A. Dey, Y. Modarres-Sadeghi and J. P. Rothstein, *J. Fluid Mech.*, 2017, **813**, R5.
19 A. A. Dey, Y. Modarres-Sadeghi and J. P. Rothstein, *Phys. Rev. Fluids*, 2018, **3**, 063301.
20 C. C. Hopkins, S. J. Haward and A. Q. Shen, *Small*, 2019, 1903872.
21 P. Flory, *Principles of Polymer Chemistry*, Cornell University Press, Ithaca, 1953.
22 P. Mitchell, *Nat. Biotechnol.*, 2001, **19**, 717.
23 L. E. Rodd, T. P. Scott, D. V. Boger, J. J. Cooper-White and G. H. McKinley, *J. Non-Newtonian Fluid Mech.*, 2005, **129**, 1–22.
24 C. J. Pipe and G. H. McKinley, *Mech. Res. Commun.*, 2009, **36**, 110–120.
25 J. A. Pathak, D. Ross and K. B. Migler, *Phys. Fluids*, 2004, **16**, 4028–4034.
26 L. Rodd, J. Cooper-White, D. Boger and G. McKinley, *J. Non-Newtonian Fluid Mech.*, 2007, **143**, 170–191.
27 S. J. Haward, R. J. Poole, M. A. Alves, P. J. Oliveira, N. Goldenfeld and A. Q. Shen, *Phys. Rev. E*, 2016, **93**, 031101.
28 L. Xi and M. D. Graham, *J. Fluid Mech.*, 2009, **622**, 145–165.
29 J. Soulages, M. Oliveira, P. Sousa, M. Alves and G. McKinley, *J. Non-Newtonian Fluid Mech.*, 2009, **163**, 9–24.
30 S. J. Haward, N. Kitajima, K. Toda-Peters, T. Takahashi and A. Q. Shen, *Soft Matter*, 2019, **15**, 1927–1941.
31 J. Zilz, R. J. Poole, M. A. Alves, D. Bartolo, B. Levaché and A. Lindner, *J. Fluid Mech.*, 2012, **712**, 203–218.
32 R. Attia, D. C. Pregibon, P. S. Doyle, J.-L. Viovy and D. Bartolo, *Lab Chip*, 2009, **9**, 1213–1218.
33 M. S. Cheri, H. Latifi, J. Sadeghi, M. S. Moghaddam, H. Shahraki and H. Hajghassem, *Analyst*, 2014, **139**, 431–438.
34 W. Li, G. Huang, J. Wang, Y. Yu, X. Wu, X. Cui and Y. Mei, *Lab Chip*, 2012, **12**, 2322–2328.

35 J. T. Pham, A. Morozov, A. J. Crosby, A. Lindner and O. du Roure, *Phys. Rev. E: Stat., Nonlinear, Soft Matter Phys.*, 2015, **92**, 011004.
36 H. Elahi, M. Eugeni and P. Gaudenzi, *Energies*, 2018, **11**, 1850.
37 H. C. Fu, C. W. Wolgemuth and T. R. Powers, *Phys. Fluids*, 2009, **21**, 033102.
38 J. Kongthon, J.-H. Chung, J. Riley and S. Devasia, *J. Dyn. Syst., Meas., Control*, 2011, **133**, 051012.
39 S. Sareh, J. Rossiter, A. Conn, K. Drescher and R. E. Goldstein, *J. R. Soc., Interface*, 2013, **10**, 20120666.
40 J. Alvarado, J. Comtet, E. De Langre and A. E. Hosoi, *Nat. Phys.*, 2017, **13**, 1014–1019.
41 D. Dendukuri, S. S. Gu, D. C. Pregibon, T. A. Hatton and P. S. Doyle, *Lab Chip*, 2007, **7**, 818–828.
42 H. Berthet, O. du Roure and A. Lindner, *Appl. Sci.*, 2016, **6**, 385.
43 J. S. Wexler, P. H. Trinh, H. Berthet, N. Quennouz, O. du Roure, H. E. Huppert, A. Lindner and H. A. Stone, *J. Fluid Mech.*, 2013, **720**, 517–544.
44 J. Cappello, M. Bechert, C. Duprat, O. du Roure, F. M. C. Gallaire and A. Lindner, *Phys. Rev. Fluids*, 2019, **4**, 034202.
45 N. Quennouz, M. Shelley, O. Du Roure and A. Lindner, *J. Fluid Mech.*, 2015, **769**, 387–402.
46 W. Weaver Jr, S. P. Timoshenko and D. H. Young, *Vibration problems in engineering*, John Wiley & Sons, 1990.
47 S. L. Anna and G. H. McKinley, *J. Rheol.*, 2001, **45**, 115–138.
48 S. Sur and J. Rothstein, *J. Rheol.*, 2018, **62**, 1245–1259.
49 L. E. Rodd, D. Lee, K. H. Ahn and J. J. Cooper-White, *J. Non-Newtonian Fluid Mech.*, 2010, **165**, 1189–1203.
50 M. Y. Hwang, H. Mohammadigoushki and S. J. Muller, *Phys. Rev. Fluids*, 2017, **2**, 043303.
51 X. Shi, S. Kenney, G. Chapagain and G. F. Christopher, *Rheol. Acta*, 2015, **54**, 805–815.
52 S. J. Haward, *Biomicrofluidics*, 2016, **10**, 043401.
53 A. Groisman and V. Steinberg, *Nature*, 2000, **405**, 53–55.
54 A. Groisman and V. Steinberg, *New J. Phys.*, 2004, **6**, 29.
55 P. Sousa, F. Pinho and M. Alves, *Soft Matter*, 2018, **14**, 1344–1354.
56 D. Boger and R. Binnington, *J. Rheol.*, 1994, **38**, 333–349.
57 J. P. Rothstein and G. H. McKinley, *J. Non-Newtonian Fluid Mech.*, 2001, **98**, 33–63.
58 R. Evans and K. Walters, *J. Non-Newtonian Fluid Mech.*, 1989, **32**, 95–105.
59 J. P. Rothstein and G. H. McKinley, *J. Non-Newtonian Fluid Mech.*, 1999, **86**, 61–88.
60 C. Li, B. Thomases and R. D. Guy, *Phys. Rev. Fluids*, 2019, **4**, 031301.
61 F. P. Beer, E. R. Johnston Jr, J. T. Dewolf and D. Mazurek, *Mechanics of Materials*, McGraw-Hill Education, 2014.
62 C. Duprat, H. Berthet, J. S. Wexler, O. du Roure and A. Lindner, *Lab Chip*, 2014, **15**, 244–252.